



n-Heptane hydroisomerization over Pt/MFI zeolite nanosheets: Effects of zeolite crystal thickness and platinum location

Jeongnam Kim^{b,1}, Wookdong Kim^{a,b,1}, Yongbeom Seo^{a,b}, Jeong-Chul Kim^{a,c}, Ryong Ryoo^{a,b,*}

^a Center for Nanomaterials and Chemical Reactions, Institute for Basic Science, Daejeon 305-701, Republic of Korea

^b Department of Chemistry, KAIST, Daejeon 305-701, Republic of Korea

^c Graduate School of Nanoscience and Technology (WCU), KAIST, Daejeon 305-701, Republic of Korea

ARTICLE INFO

Article history:

Received 14 May 2012

Revised 30 January 2013

Accepted 13 February 2013

Available online 20 March 2013

Keywords:

Hierarchical zeolite

Bifunctional catalyst

Hydroisomerization

Heptane

Zeolite thickness

Metal location

Platinum nanoparticle

ABSTRACT

Platinum was supported on MFI-type (ZSM-5) zeolites with various crystal thicknesses ranging from 300 to 2 nm (i.e., from bulk crystal to nanosheet). Two series of Pt/MFI were prepared by the ion exchange of $\text{Pt}(\text{NH}_3)_4^{2+}$ and the impregnation of colloidal Pt nanoparticles. The ion exchange yielded Pt nanoparticles that were supported inside zeolite pores, whereas the impregnation yielded Pt nanoparticles supported exclusively on the external crystal surfaces. The two series of Pt/MFI were used as catalysts for the hydroisomerization of *n*-heptane to investigate the effects of zeolite crystal thickness and Pt location. This research showed that the product selectivity to branched isomers could be significantly improved by decreasing zeolite crystal thickness to nanosheets. The selectivity improvement was attributed to short diffusion path lengths for branched products to escape before cracking.

© 2013 Elsevier Inc. All rights reserved.

1. Introduction

Liquid *n*-alkanes are important precursors for transportation fuels that can be obtained from petroleum distillation, Fischer-Tropsch synthesis, and bio-oil deoxygenation [1]. However, such linear hydrocarbons have poor fuel properties (e.g., low octane numbers in gasoline) that require additional refining processes. Selective hydroisomerization is a well-known process for improving the fuel quality of *n*-alkanes by converting them into branched isomers [2–4]. A typical catalyst for this process is bifunctional, consisting of a noble metal (e.g., Pt or Pd) dispersed on an acidic support. The metal component catalyzes the generation of intermediate olefins via dehydrogenation and the formation of products via hydrogenation. The acidic sites are responsible for generating carbenium ions from olefins for isomerization [4]. Among the catalysts developed so far, Pt-loaded aluminosilicate zeolites are widely used in commercial processes due to their strong acidity, high metal dispersion, and shape-selective micropores [2–4]. However, the presence of uniform micropores (<2 nm) in micrometer-sized crystals often imposes slow mass transfer, leading to low

catalytic efficiency during reactions. Continuous efforts have been devoted to overcome this diffusion limitation and to improve the catalytic process [5–7].

Diffusion in zeolites can be improved by shortening the diffusion path lengths via the synthesis of nanocrystalline zeolites or by the generation of mesopores within a zeolite crystal. Zeolites resulting from both approaches have been investigated in *n*-alkane hydroisomerization reactions in the past. For example, Chica and Corma supported Pt nanoparticles (NPs) on nanocrystalline beta zeolite of ~30 nm in diameter [8]. Additionally, De Jong and Koningsberger supported Pt on mordenite zeolite after the generation of mesopores [9,10]. There are other studies employing various methods to generate mesopores in zeolites [11–14] and to delaminate zeolite into nanosheets [15]. These zeolite catalysts, supporting Pt metals, exhibited significant improvements of selectivity in *n*-alkane hydroisomerization compared to bulk zeolite. Thus, small zeolite crystal sizes were paramount to improve branched hydrocarbon selectivity.

The location of Pt metal is important in bifunctional catalysts. Since the introduction of the bifunctional concept by Weisz [16], it has been suggested that the metal and acid sites should be as near as possible for high catalytic activity and selectivity [17]. In this respect, methods to support Pt NPs uniformly, such as the ion-exchange (IE) technique, are widely used in the preparation of bifunctional Pt/zeolite catalysts [18]. There are some cases in which Pt NPs and acid catalytic sites are bifunctional without close

* Corresponding author at: Center for Nanomaterials and Chemical Reactions, Institute for Basic Science, Daejeon 305-701, Republic of Korea. Fax: +82 42 350 8130.

E-mail address: rryoos@kaist.ac.kr (R. Ryoo).

¹ These authors contributed equally to this work.

contact. In these cases, the rapid transfer of reaction intermediates via surface or gas-phase diffusion is known to allow the kinetic coupling between two detailed catalytic processes over a distance, leading to a sequential bifunctional pathway [19]. Numerous attempts have been made to understand the distance effects using a physical mixture of individual catalytic components such as Pt/SiO₂ and acidic zeolite. Often, the Pt catalyst is supported on non-acid silica, while the acid components are located in the zeolite particles [16,20–22]. The metal-to-acid site distances are not precisely controlled in this case. The distance between Pt and the acid would be more precisely controlled if Pt NPs could be supported on the external surfaces of a zeolite particle with a well-defined thickness. It would therefore be interesting to try a series of acidic zeolites with extremely well-defined crystal sizes over a wide range, decreasing the crystal thickness down to only a few nanometers.

Owing to the development of zeolite synthesis strategies using zeolite structure-directing surfactants, ultrathin zeolite nanosheets of a single unit cell thickness can now be synthesized (~2 nm) [23–25]. This has provided the opportunity to extend the investigation of zeolite crystal size on *n*-alkane hydroisomerization selectivity down to the 2-nm scale. Zeolite nanosheets with well-defined thicknesses can support Pt NPs inside the internal micropores following the IE method. It is also possible to support Pt NPs exclusively on the external surfaces of the nanosheet using the colloid impregnation (CI) method [26,27]. In the CI method, Pt NPs of uniform diameter are prepared in a colloidal solution. This solution is then impregnated into a porous material. The NPs can maintain their original particle diameters after the impregnation, unless the supported particle concentration is high enough to cause agglomeration. The Pt NP diameter can now be controlled over a wide range (1–100 nm) [28]. If NPs larger than 1.5 nm are used, these NPs can be exclusively supported on the external crystal surfaces of zeolite because they are too large to enter zeolite micropores (~0.55 nm).

The present work was undertaken to investigate the effects of single-unit-cell-sized zeolite crystal thickness and Pt location in relation to acid sites on linear alkane hydroisomerization. To address these points, we synthesized conventional ZSM-5 with approximately 300-nm crystal thickness, nanocrystalline MFI (~10 nm), and MFI nanosheets with 2-nm thickness along the *b*-axis. To support Pt NPs on these zeolites, we used two different preparation methods: conventional IE and the recently developed CI. The supported Pt catalysts were characterized by hydrogen chemisorption and transmission electron microscopy (TEM). The catalytic performance of these Pt-supporting zeolites for hydroisomerization was investigated using *n*-hexane (*n*-C₆) and *n*-heptane (*n*-C₇) as substrates, reflecting the importance of upgrading light naphtha components [8]. The investigation was focused on *n*-C₇, due to its higher tendency to crack than *n*-C₆ [29]. The result of the catalytic investigation was analyzed in terms of zeolite crystal thickness and Pt location.

2. Experimental

2.1. Zeolite preparation

2.1.1. Zeolite synthesis

The 2-nm thick MFI zeolite nanosheets were synthesized using a compound with a molecular formula of C₁₆H₃₃-N⁺(CH₃)₂-C₆H₁₂-N⁺(CH₃)₂-C₆H₁₃(Br⁻)₂ [C₁₆₋₆₋₆(Br)₂] as a structure-directing agent (SDA), following a procedure described previously [24]. In brief, water glass with a Si/Na ratio of 1.75 was used as the silica source, and sodium aluminate was used as the alumina source. The molar composition of the starting mixture was 100 SiO₂:1 Al₂O₃:7.5

C₁₆₋₆₋₆(Br)₂:30 Na₂O:24 H₂SO₄:4000 H₂O. The mixture was heated in a Teflon-lined autoclave with tumbling in an oven at 413 K for 7 d. The zeolite product was collected after filtration, washing with water, and drying at 373 K. The zeolite thus obtained was calcined at 823 K in air. The zeolite was ion-exchanged three times with 1 M NH₄NO₃ solution and subsequently calcined again at 823 K for its full conversion to the H⁺ form. This sample is denoted “NS-2” in the text.

Nanocrystalline MFI zeolite of ~10 nm was synthesized with a diammonium-type SDA, C₃H₇-N⁺(CH₃)₂-C₆H₁₂-N⁺(CH₃)₂-C₃H₇(Br⁻)₂ [C₃₋₆₋₃(Br)₂] following the procedure reported by Na et al. [30], except the synthesis temperature (423 K) and the starting molar composition (100 SiO₂:0.083 Al₂O₃:10 C₃₋₆₋₃(Br)₂:30 Na₂O:15 H₂SO₄:6000 H₂O). The zeolite was also converted to the H⁺ form in the same manner used for NS-2. This zeolite is denoted by “NC-10” in the text.

Bulk zeolite with an approximately 300-nm crystal thickness was obtained with tetrapropylammonium hydroxide (TPAOH). The starting mixture had a molar composition of 100 SiO₂:1 Al₂O₃:30 TPAOH:3 H₂SO₄:6000 H₂O. Tetraethylorthosilicate (TEOS, 95%, Junsei) was used as the silica source, and aluminum sulfate [Al₂(SO₄)₃·18H₂O, 98%, Sigma-Aldrich] was used as the alumina source. In a typical synthesis, 0.67 g of Al₂(SO₄)₃·18H₂O was dissolved in 114 g aqueous TPAOH solution (5.4 wt.%). To this solution, 20.8 g of TEOS was added with magnetic stirring. The mixture was heated to 333 K, and stirring was continued for 6 h. The sol-like clear mixture was heated in a Teflon-lined autoclave at 443 K for 2 d under static conditions. The resultant zeolite product was collected and treated in the same manner as for NS-2. This sample is denoted as “B-300” in the text, which means “bulk crystals with 300-nm thickness”.

A commercial MFI zeolite in the NH₄⁺ form was purchased from Zeolyst (CBV8014, SiO₂/Al₂O₃ = 80) and calcined at 823 K before use. The zeolite was composed of aggregated nanosize crystals with a wide distribution of thicknesses from 20 to 50 nm (see Section 3.1 for detailed characterization). This sample is designated as “C-40” in the text, where “C” means “commercial” and “40” stands for its mean crystal thickness.

2.1.2. Platinum loading

The IE method was applied in the following manner [31–33]. Briefly, 1.0 g of zeolite was added to a 20 mL aqueous solution containing 0.0202 g of Pt(NH₃)₄(NO₃)₂ (98%, Sigma-Aldrich). The slurry was magnetically stirred overnight at room temperature. Afterward, the zeolite was filtered, washed with deionized water, and dried at 373 K. The zeolite powder was placed on a fritted disk inside a Pyrex U-tube flow reactor, heated to 623 K at a ramping rate of 0.4 K min⁻¹, and kept at this temperature for 2 h under flowing dry oxygen (>1 L min⁻¹ g⁻¹ zeolite). The activated sample was treated in flowing H₂ (>200 mL min⁻¹ g⁻¹) with linear heating to 573 K for 4 h and holding for 2 h. The sample was subsequently degassed at 573 K for 2 h to remove chemisorbed hydrogen.

The CI method was used in the same manner as reported by the Somorjai group [26], except for the use of octylamine (99%, Sigma-Aldrich) as an organic-capping agent. Pt NPs exhibiting a particle size distribution of 1.4 ± 0.3 nm (see Section 3.1) were prepared by adding an ethylene glycol solution of NaOH (10 mL, 0.5 M) to a 10 mL ethylene glycol solution containing 0.2 g of H₂PtCl₆ (37.5 wt.% Pt, Heesung Metal) [34]. The mixture was heated at 413 K for 3 h under vigorous stirring with N₂ bubbling. The resultant dark-brown colloidal solution was mixed with 1.23 mL of octylamine (N/Pt molar ratio of 20) dissolved in toluene (15 mL). Ethanol was added to this mixture to provide a homogeneous colloidal solution. Fifty milliliters of deionized water was added to this solution, and the solution was mixed by shaking. The colorless aqueous layer was discarded, and the organic layer containing the

Pt NPs was collected and diluted with 15 mL of ethanol solution containing 0.53 mL of 2 M hydrochloric acid (for an HCl/octylamine molar ratio of 1). After shaking, this solution was washed with 50 mL of deionized water. Washing was repeated three times to remove excess octylamine. The concentration of the dispersed Pt NPs in the resultant organic solution was approximately 0.77 wt.%.

In a typical experiment, 1 g of zeolite was impregnated with 1.31 g of colloidal Pt solution and rubbed with a Teflon-coated spatula for uniform distribution of the Pt. After drying at 333 K, the Pt-impregnated zeolite was heated in Pyrex tubing equipped with fritted disks at 573 K for 1 h under flowing O₂. After the O₂ flow was stopped, the sample tubing was degassed for 30 min at the same temperature. The sample was further treated with a cycle of H₂ contact (~400 Torr, static), degassing, O₂ contact (~400 Torr), and degassing, with a dwell time of 30 min at 573 K for each step. The entire cycle was repeated two more times to ensure complete removal of amine from the Pt surfaces by oxidation.

2.2. Catalyst characterization

The Si/Al ratios and Pt content were determined by inductively coupled plasma-atomic emission spectroscopy (ICP-AES) using an OPTIMA 4300 DV instrument (Perkin Elmer). X-ray diffraction patterns (XRD) were collected between 2 θ angles of 5° and 35° with a Rigaku Multiflex diffractometer using Cu K α radiation. The set voltage and current were 30 kV and 40 mA, respectively. Scanning electron microscope (SEM) images were obtained with an FEI Nova 230 instrument operating at 2 kV. TEM images were taken with a Tecnai G2 F30 instrument with an accelerating voltage of 300 kV. Scanning transmission electron microscope (STEM) images were taken with a spherical aberration corrected JEM-ARM200F with an accelerating voltage of 200 kV. Nitrogen adsorption isotherms were obtained at the temperature of liquid nitrogen (77 K) using a volumetric Micromeritics Tristar-II instrument. Prior to the measurements, the sample was degassed for 12 h at 573 K. The specific surface area was calculated by the Brunauer–Emmett–Teller (BET) equation using the adsorption data obtained in the pressure range $P/P_0 = 0.05$ – 0.2 .

The temperature programmed desorption of ammonia (NH₃ TPD) was measured using a BELCAT-M (BEL Japan) instrument equipped with a thermal conductivity detector (TCD). The NH₃ adsorption was carried out at 373 K. The TPD profile was obtained while heating from 373 to 923 K at a ramping rate of 10 K min⁻¹ under flowing helium (30 mL min⁻¹). The TPD profile was deconvoluted with the assumption of Gaussian distributions. The higher temperature peak (600–800 K) in the profile was used to estimate the number of strong acid sites with the assumption of one NH₃ molecule per acid site [35].

Solid-state ³¹P NMR spectra were acquired using magic angle spinning (MAS) with a Bruker AVANCE400WB spectrometer at room temperature. Before acquiring ³¹P NMR measurements, each zeolite sample was dehydrated under vacuum at 573 K. The sample was added with a methylene chloride solution containing a known amount of trimethylphosphine oxide (TMPO), following the method reported in the literature [36,37]. Subsequently, methylene chloride was removed by evacuation at room temperature. The sample with phosphine oxide was transferred into an NMR spectroscopic sample rotor which had a gas-tight cap inside a glove box. Then, ³¹P MAS NMR spectra were acquired by way of a single-pulse sequence with a pulse width of 2 μ s, a relaxation time of 5 s and a spinning frequency of 12 kHz. An 85% aqueous solution of H₃PO₄ was used as an external standard. A Gaussian deconvolution method was used to analyze the ³¹P NMR spectrum [37]. The P content was analyzed from the same sample by ICP/AES.

Hydrogen chemisorption isotherms were obtained at room temperature using a lab-made volumetric adsorption apparatus.

Before measurements, the Pt-loaded sample was reduced at 573 K in flowing H₂ (99.999%, passed through a MnO/SiO₂ trap). The hydrogen chemisorption in H/Pt was determined by extrapolation of the adsorption isotherm to zero pressure. This value refers to the total chemisorption. The Pt dispersion was calculated with the assumption of one hydrogen atom per surface Pt in the chemisorption [39].

2.3. Catalytic reaction measurement

The *n*-C₇ hydroisomerization reaction was carried out in a continuous-flow Pyrex reactor (inner diameter = 13 mm) under H₂ at atmospheric pressure using 0.1 g of powdered catalyst. The temperature was measured using a K-type thermocouple inserted into the reactor through a thermocouple well. Prior to the reaction, the catalyst was reduced with high-purity H₂ (99.999%, 22 mL min⁻¹) at 573 K for 2 h. After cooling to 473 K, *n*-C₇ (99 + %, Junsei) was fed through a syringe pump (KD Scientific) with a H₂/*n*-C₇ molar ratio of 10. The weigh hourly space velocity (WHSV) of *n*-C₇ was 6.8 h⁻¹. The reactor was heated with a furnace controlled over the range of 473–573 K. The reaction effluent was analyzed using an online gas chromatograph (GC, Younglin, Acme-6000) equipped with a flame ionization detector. The products were separated by a 50 m \times 0.32 mm fused-silica capillary column (SUPELCO Petrocol DH50.2). After stabilization at a target reaction temperature, a reaction analysis by GC was repeated three times to obtain an average. The reaction was then switched to a new temperature while holding the reactant flow constant. Hydroisomerization of *n*-C₆ (96%, Junsei) was performed, following the same procedure used for *n*-C₇, except for the difference in reaction temperature (513–603 K) and the use of reactant WHSV (6.5 h⁻¹). The products were separated by a capillary column (J&W GS-GasPro).

3. Results and discussion

3.1. Structures and properties of the catalytic materials

3.1.1. Zeolite crystals of various thicknesses

Four samples of MFI zeolite with various crystal thicknesses were obtained as described in Section 2.1. These samples were designated B-300, C-40, NC-10, and NS-2, where the numbers after the hyphens refer to the crystal thickness (nm) in the thinnest dimension (see below). Except for NS-2, the crystal thicknesses were estimated from SEM images. High-resolution TEM images had to be used in the case of the thin nanosheet NS-2 [23]. Representative SEM and TEM images are shown in Fig. 1. From the SEM images, the laboratory-made B-300 bulk zeolite sample exhibited a wide distribution of crystal diameters ranging from 500 to 1000 nm. These crystal diameters were measured along the longest crystal dimension. However, in view of the mass transfer problems in catalysis, it is appropriate to measure crystal size along the thinnest dimension. The crystal size of the B-300 sample measured in this manner showed a distribution from 250 to 350 nm, averaging approximately 300 nm. The crystal size at the center is referred to as the “crystal thickness” in discussions hereafter.

In the case of the C-40 commercial zeolite sample, the SEM image in Fig. 1b shows the aggregation of primary crystals with a wide distribution of diameters ranging from 40 to 150 nm. The crystal thickness was thus estimated to be 40 nm. NC-10 shows a relatively narrow distribution of 20–40 nm for crystal diameters [30], while the crystal thickness of NC-10 was 10 nm. NS-2 exhibited sponge-like morphologies composed of very thin nanosheets. High-resolution TEM investigation revealed that NS-2 was obtained in the form of a highly disordered assembly of nanosheets

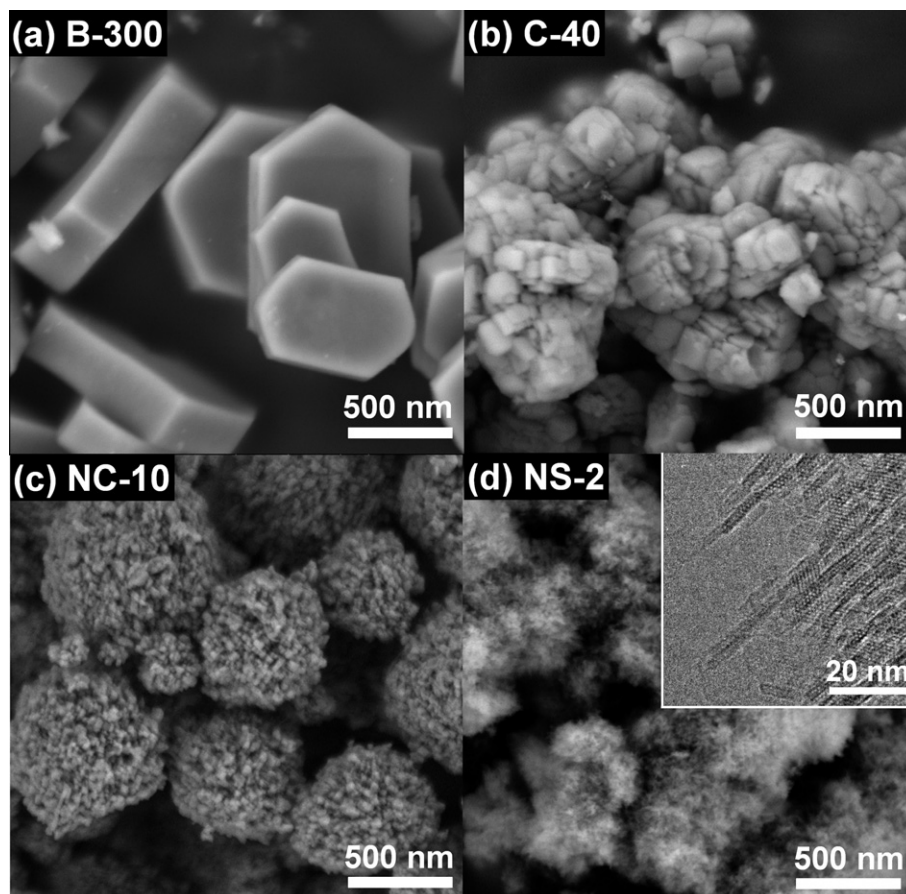


Fig. 1. Representative SEM and TEM images obtained from (a) B-300, (b) C-40, (c) NC-10, and (d) NS-2 samples.

Table 1
Characteristics of the MFI zeolite supports used in the present work.

Support ^a	Si/Al	S_{BET} ($\text{m}^2 \text{g}^{-1}$)	N_{acid} (mmol g^{-1})	BA_{86} (mmol g^{-1})	BA_{76} (mmol g^{-1})
B-300	50	360	0.15	0.046	0.13
C-40	42	400	0.23	0.060	0.17
NC-10	43	420	0.22	0.067	0.14
NS-2	43	630	0.16	0.017	0.12

^a Si/Al ratio determined from ICP-AES; S_{BET} is the BET surface area; N_{acid} is the number of strong acid sites determined from the 573 to 773 K peak in the NH_3 TPD profile. BA_{86} and BA_{76} are the number of strong Brønsted acid sites determined from the 86 ppm and 76 ppm peak in the ^{31}P MAS NMR spectra of TMPO, respectively.

with an ac plane diameter of approximately 20 nm and a thickness of 2 nm along the b -axis [23].

Amorphous particles or other impurities were not detected by SEM or TEM in the present zeolite samples. The crystalline structure of MFI zeolite was confirmed by XRD patterns exhibiting Bragg diffraction peaks (Fig. S1, Supporting information). All peaks were assignable to the crystalline MFI zeolite structure. The peak intensities decreased in the order of B-300 > C-40 > NC-10 > NS-2, while XRD line widths changed inversely. This order was consistent with decreasing crystal thickness. In NS-2, the XRD pattern exhibited only ($h0l$) reflections, which was consistent with the thickness corresponding to a single unit dimension along the b -axis [23]. No broad peaks attributable to amorphous impurities were detected in the 2θ range of 15–25°.

The BET area, Si/Al ratios, and concentrations of strong acid sites are summarized in Table 1. The specific BET surface area increased in the order of B-300 < C-40 < NC-10 << NS-2. The NS-2 sample had a specific surface area ($630 \text{ m}^2 \text{g}^{-1}$) twofold higher than B-300 and also quite a large mesopore volume ($0.65 \text{ cm}^3 \text{g}^{-1}$). This was due to

the presence of mesopores between the nearest neighboring nano-sheets in NS-2 [23,24]. All samples were prepared to have similar Si/Al ratios within the range of 42–50. The number of strong acid sites, shown in Table 1, was calculated from the high-temperature desorption peak (573–773 K) in the NH_3 TPD profile (Fig. S2, Supporting information). This desorption peak can be attributed to NH_3 desorption from strong Brønsted and Lewis acid sites. However, the NH_3 TPD profile is insufficient to provide accurate information about the strength of the acid sites. Moreover, the role of Lewis acid sites on the hydroisomerization of n -paraffins is still in debate [38]. For this reason, the Brønsted acid sites were further analyzed by solid-state ^{31}P NMR spectroscopy using trimethylphosphine oxide (TMPO) as a probe molecule, which was developed by Rakiewicz et al. [36]. According to the ^{31}P NMR spectroscopic method, TMPO is a basic molecule that can be strongly adsorbed on a Brønsted acid site in zeolitic frameworks. The ^{31}P NMR chemical shift increases according to acid site binding affinity. Owing to these characteristics, the ^{31}P NMR spectroscopic method is suitable for a quantitative analysis of zeolite acidic sites.

Our analysis by ^{31}P NMR spectroscopy revealed four NMR peaks (86, 76, 68, and 64 ppm) corresponding to TMPO adsorbed on Brönsted acid sites (see Fig. S3, Supporting information). Among these, the two peaks appearing at 68 and 64 ppm can be assigned to TMPO adsorbed on weak Brönsted acid sites as they are also present in amorphous aluminosilicate MCM-41 [37]. The other peaks (86 and 76 ppm) are attributed to the presence of two types of strong Brönsted acid sites in the MFI zeolite. The concentrations of these acid sites are given in Table 1. Based on this result, it can be concluded that all the present zeolitic samples possessed similar concentrations of strong Brönsted acid sites, except for the low concentration of the strongest acid sites (86 ppm) in NS-2. However, it is uncertain if both types of acid sites (86 and 76 ppm) or only the stronger acid sites (86 ppm) were catalytic for *n*-alkane hydroisomerization.

3.1.2. Pt NPs supported by IE

Careful treatment after $\text{Pt}(\text{NH}_3)_4^{2+}$ ion exchange is crucial for the preparation of highly dispersed Pt NPs in MFI zeolites, including extremely thin NS-2. As emphasized previously [18,31–33], slow heating ($<0.5\text{ K min}^{-1}$) under fast flow of dry O_2 ($>1\text{ L min}^{-1}$) is of prime importance during the pretreatment process. This procedure allows Pt precursors to fully convert into Pt^{2+} ions coordinated to the zeolitic framework. As a result, the IE sample turned pale green after O_2 treatment. These resultant Pt species were able to form very small Pt particles, which were occluded mainly inside the zeolite micropores after treatment with H_2 [32,33].

Representative STEM and TEM images for B-300 and NS-2 prepared by IE are shown in Fig. 2. As the images show, small Pt NPs were uniformly supported on these MFI zeolites. The diameters of the Pt NPs were approximately 1 nm with a narrow size distribution. Careful investigation of the zeolite crystal edges by STEM revealed that the B-300 sample had Pt NPs located mostly inside crystals (see Fig. S4, Supporting information). These Pt NPs were larger than the cross-sectional diameter of the microporous channels ($\sim 0.55\text{ nm}$). The presence of such larger Pt NPs seemed to involve local destruction of the zeolite framework, as suggested in earlier investigations [32,42]. In the case of NS-2, it seemed that quite a significant number of Pt NPs were located on external surfaces of the zeolite nanosheets.

As shown in Table 2, the Pt loading by IE was carefully controlled to give similar contents of Pt (0.87–0.99 wt.%) for all samples. All IE samples gave very similar results for hydrogen chemisorption within the range of $\text{H}/\text{Pt} = 1.07\text{--}1.41$. These H/Pt ratios were greater than unity, violating the assumption of the surface stoichiometry of $\text{H}/\text{Pt}_{\text{surface}} = 1$ [36]. This is not surprising, however, as there are many reports on hydrogen chemisorption of $\text{H}/\text{Pt} > 1$ when Pt metal is supported on zeolites [31,40,41]. The equation of $d\text{ (nm)} = 1.13/D$, where D is the Pt dispersion, is conventionally used to calculate Pt NP diameters. This equation assumes spherical particles, $\text{H}/\text{Pt}_{\text{surface}} = 1$, and a Pt atom density of $1.25 \times 10^{19}\text{ atoms m}^{-2}$. Particle diameters calculated using this equation are in very good agreement with diameters determined by STEM in the region of $d > 3\text{ nm}$. However, the two methods differed significantly as the particle diameter decreased below 1.5 nm. The difference could

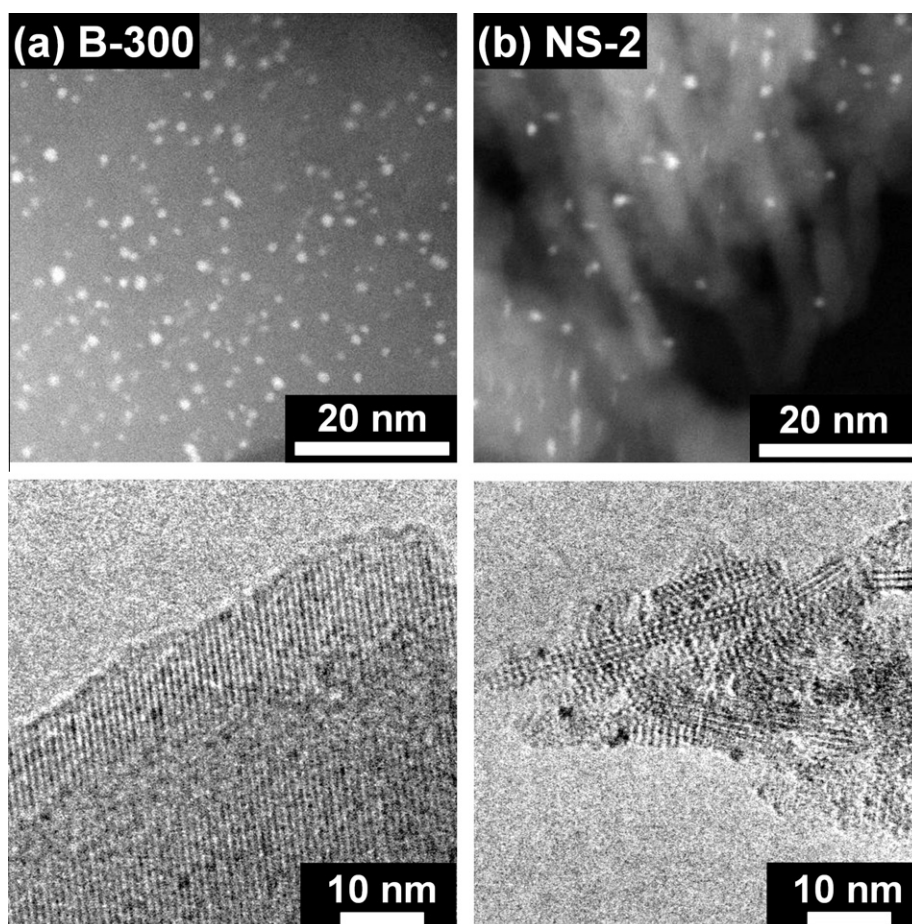


Fig. 2. STEM and TEM images of (a) Pt-loaded B-300 and (b) NS-2 prepared using the IE method. The Pt particles ($\sim 1\text{ nm}$ in diameter) are highly dispersed on MFI zeolites regardless of the framework thickness.

Table 2
Characteristics of the Pt/MFI zeolites prepared using IE and CI methods.

Catalyst ^a	Method	Pt (wt.%)	H/Pt	d_{chem} (nm)	d_{TEM} (nm)
B-300	IE	0.87	1.41	0.8	1.2 ± 0.3
	CI	0.90	0.36	3.1	3.2 ± 0.7
C-40	IE	0.99	1.08	1.0	–
	CI	0.81	0.40	2.8	3.0 ± 0.6
NC-10	IE	0.90	1.07	1.1	–
	CI	0.88	0.52	2.5	2.5 ± 0.5
NS-2	IE	0.95	1.14	1.0	1.0 ± 0.3
	CI	0.91	0.70	1.6	1.8 ± 0.3
	CI*	0.90	0.50	2.3	2.8 ± 0.4

^a IE = ion exchange; CI = colloidal impregnation; Pt content determined from ICP-AES; H/Pt ratio refers to the total chemisorption value measured at room temperature; d_{chem} is the mean particle diameters calculated according to equation $d = 1.13/D$, where D is the metal dispersion; d_{TEM} is the mean particle diameter determined by counting a minimum of 150 particles.

be explained by changing the surface stoichiometry [41]. As the particle size decreases below 2 nm, nanoparticles have relatively more edge and corner atoms than large particles. Such low-coordinated atoms could chemisorb more than 1 H atom.

3.1.3. Pt NPs supported by CI

The CI method, which was used by the Somorjai group, was modified in the present work [26,27]. The previous method employed poly(vinylpyrrolidone) as a capping agent. However, the surrounding polymer layer caused the overall Pt NP diameters to increase to sizes that were too large to enter mesopores in the NS-2 sample. For this reason, the poly(vinylpyrrolidone) was replaced with octylamine. The Pt NPs capped with octylamine could be distributed uniformly over the zeolite surface without sonication, which can destroy the support material [43]. However, octylamine has the disadvantage of catalyst poisoning. To reduce the amine concentration in the colloidal solution before impregnation, any octylamine remaining after the NP capping was removed by neutralization with HCl and subsequent washing. Amine removal was confirmed by thermogravimetric analysis (TGA). Without amine removal, a weight loss corresponding to the amine was detected in TGA at temperatures above 573 K. After acid treatment and washing, the TGA signal disappeared almost completely. The excess amine was removed in this manner, but the sample still contained some amine molecules that were capping Pt surfaces. These organic amines are known to be a strong poison to Pt surfaces in addition to poisoning acid sites. Because amines are not easily removed even by calcination in O₂ at 573 K [44], our samples had to be treated with O₂ and H₂ repeatedly at 573 K to remove the Pt-capping amine before use.

The platinum content of the CI samples was controlled to have similar values within the range of 0.81–0.91 wt.% (Table 2). Fig. 3 shows representative TEM images of Pt NPs taken before and after impregnation into zeolite samples. The image in Fig. 3a was taken from TEM grids after the deposition of Pt NPs from the initial colloidal solution. As can be observed, the diameters of the Pt NPs were within the range of 1.4 ± 0.3 nm. After being supported on zeolite samples, however, the particle diameters increased to 3.2 ± 0.7 in the case of B-300, 3.0 ± 0.6 in C-40, 2.5 ± 0.5 in NC-10, and 1.8 ± 0.3 nm in NS-2. The increased particle diameters seemed to be due to the O₂ and H₂ treatments, which were performed to remove amine at 573 K. The results indicated that particle sintering decreased as the external surface area increased or the crystal thickness decreased. This particle sintering was unavoidable, even in the case of NS-2, which had the highest specific external surface area.

The hydrogen chemisorption results are given in Table 2. The hydrogen chemisorption data indicated that the Pt metal dispersion gradually decreased with increasing zeolite crystal thickness, which was in good agreement with the TEM data (Table 2). This agreement supported the notion that the amine groups on the Pt NPs were fully removed by the O₂–H₂ treatment at 573 K.

The Pt NPs ($d = 1.4 \pm 0.3$ nm) in the colloidal solution were larger than the micropore apertures (~0.55 nm) of MFI zeolite. Therefore, the NPs would not easily diffuse into the micropores. However, if heated under oxidative conditions to high temperatures, the Pt species could diffuse via a re-dispersion process. For example, Rivallan et al. observed re-dispersion at 723 K [45]. This process involves the formation of a Pt(II) species, which diffuses into the zeolite crystal through IE. Upon subsequent reduction, Pt NPs approximately 1 nm in diameter can be found inside the zeolite crystals (i.e., in the micropores). The Pt re-dispersion was confirmed in the present work, and accordingly, the temperature for the O₂–H₂ treatments was capped at 573 K to prevent re-dispersion. Platinum NPs of less than 1 nm were not detected by STEM investigation. Nonetheless, sintering between particles occurred at the external surface. In recent years, various approaches, such as solvent extraction [46] and UV/ozone treatment [47], have been employed to solve the problems caused by thermal treatment.

The NS-2 zeolite in Table 2 shows an additional sample denoted as CI*. The Pt loading on this sample was also carried out by colloidal impregnation using Pt NPs of $d = 2.4 \pm 0.4$ nm. The colloidal solution of these Pt NPs was prepared in the same way as for the NPs used in CI (1.4 ± 0.3 nm), except for the addition of distilled water (H₂O/ethylene glycol = 0.1 by weight) [34]. The CI* procedure gave a Pt dispersion of 0.50 on the NS-2 zeolite, as determined by hydrogen chemisorption. The mean particle diameter from the chemisorption data was 2.3 nm, which was very close to the 2.8 ± 0.4 nm value obtained from TEM.

Scheme 1 represents the Pt locations and particle sizes, which depended on the type of Pt-support method (i.e., IE or CI) and zeolite crystal thicknesses. Note that in the case of the extremely thin nanosheets, a short distance between the Pt and acid sites could be maintained regardless of the preparation method. In contrast, a large difference in this distance between the IE and CI methods was observed in the conventional ZSM-5.

The IE method can provide Pt NPs close to the acid sites, while the CI method yields Pt NPs solely located on external surfaces. In the following section, we discuss *n*-C₆ and *n*-C₇ hydroisomerization results on these Pt/MFI catalysts with respect to zeolite crystal thickness and Pt locations.

3.2. *n*-C₇ hydroisomerization over Pt/MFI zeolites

3.2.1. Effect of zeolite crystal thickness in Pt(IE)/MFI catalyst series

As described in the previous section, all Pt/MFI samples had similar Pt loadings in the range of 0.81–0.99 wt.%. The Pt content was high enough to provide a hydrogenation function in the present bifunctional catalysis, assuming that the Pt metal was homogeneously supported with sufficiently high dispersion [48–50]. Hence, the Pt content was chosen for investigation of zeolite thickness effects. The catalytic reaction was performed between 473 and 573 K with reaction temperatures selected randomly, whereas there were no history effects for choosing the reaction temperatures. At least three synthesized batches of zeolite samples were used to support Pt NPs. Catalyst samples of different batches gave reproducible results within 10% relative errors in conversion, and no significant deactivation of the catalyst was detected during the entire measurements. The *n*-C₇ reactant was successfully isomerized into *i*-C₇ or cracked into smaller products. The percentage of

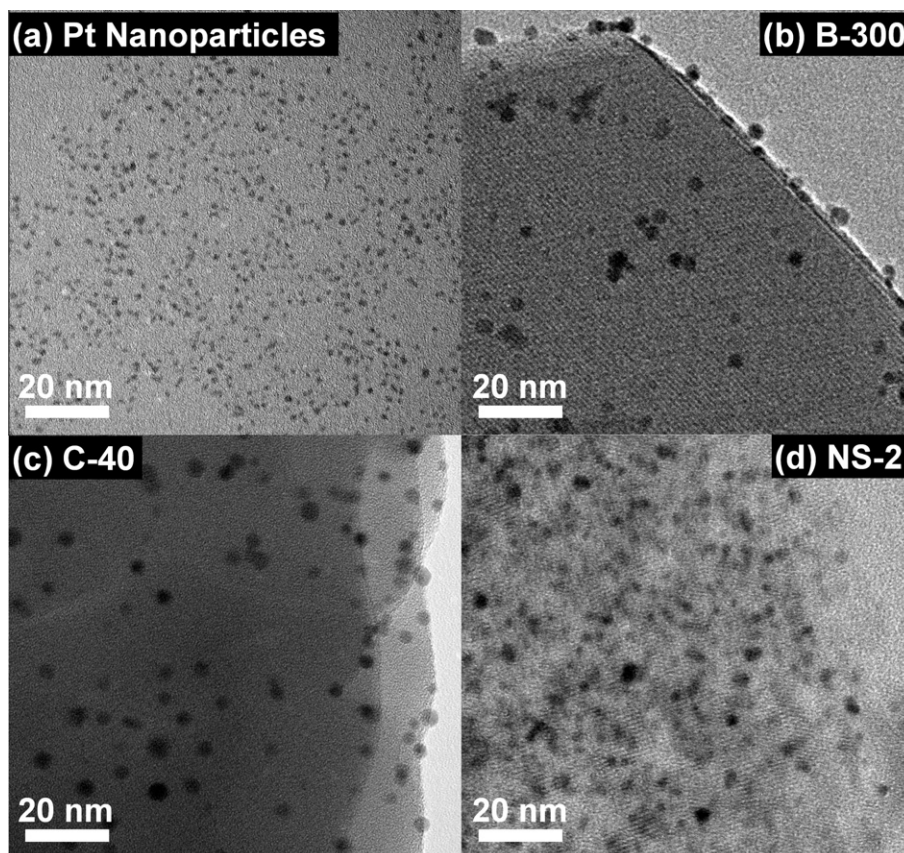
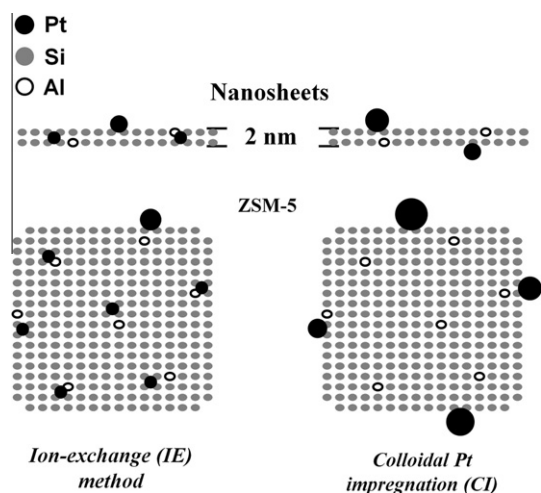


Fig. 3. High-resolution TEM images of (a) presynthesized Pt NPs (1.4 ± 0.3 nm), (b) B-300, (c) C-40, and (d) NS-2 after impregnation, calcination, and sequential O_2 - H_2 cycle at 573 K.



Scheme 1. Schematic representation of Pt locations in conventional ZSM-5 and 2-nm thick MFI nanosheets prepared by the IE and CI methods.

n - C_7 converted to these products was defined as the “ n - C_7 conversion”.

Fig. 4 shows the catalytic reaction results for the Pt/MFI samples prepared by IE. The catalytic conversion of n - C_7 was first plotted as a function of reaction temperature (Fig. 4a). The data showed very similar S-curves for the various catalysts, despite their wide variation in crystal thickness. This result indicated that the overall conversion of n - C_7 was not controlled by diffusion in these zeolitic catalysts under the present reaction conditions. The product

stream contained i - C_7 , propane, i -butane, and other various products of hydrocarbon cracking, as well as some remaining n - C_7 . The molar percentage of i - C_7 in the product stream was defined as the “ i - C_7 mole percent”. In Fig. 4b, the total conversion of n - C_7 was then placed on the x -axis. On the y -axis, the i - C_7 mole percent was plotted. Each plot in this figure showed a correlation between the total conversion and the i - C_7 mole percent for a given catalyst, which was measured over the reaction temperature range (473–573 K). Each catalyst data set showed a single maximum point in the region of 45–75% conversion. The i - C_7 mole percent increased as the crystal thickness decreased on comparing at the same level of conversion. The maximum i - C_7 mole percent was 22 mol% in the case of Pt NPs supported on the B-300 zeolite. The i - C_7 mole percent changed to 29 mol% in the case of C-40, 42% in NC-10, and 48% in NS-2. Thus, the maximum obtainable i - C_7 mole percent could be improved to 48% by decreasing the MFI zeolite crystal thickness. The most efficient catalyst was Pt(IE)/NS-2. This zeolite is comparable to beta zeolite possessing a larger pore diameter (~ 0.7 nm) that has been frequently investigated as a hydroisomerization catalyst after it is loaded with Pt NPs [8]. The Pt/beta catalyst gives a maximum i - C_7 mole percent of 48 mol% under the same conditions. However, the Pt/beta catalyst has the advantage of higher selectivity for multi-branched isomers ($\sim 20\%$).

The detailed product distribution is given in Table 3. As this result shows, the IE catalysts gave mono-branched C_7 alkanes (i.e., 2- and 3-methylhexanes) as the major isomer products. The selectivity for di -branched isomer was 7.5% in Pt/NS-2, whereas Pt/B-300 was poorly selective to di -branched isomers (0.4%). This difference between Pt/NS-2 and Pt/B-300 can be explained by product shape selectivity owing to diffusion limitations. Tri -branched isomer was not detected in any catalyst samples, which

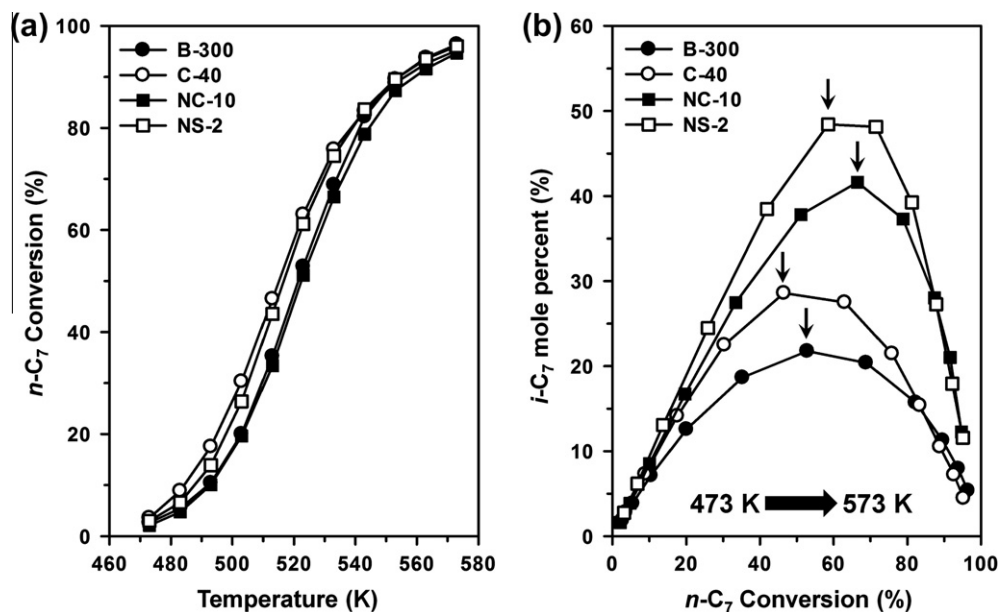


Fig. 4. (a) n -C₇ conversion by Pt(IE)/MFI catalysts plotted as a function of reaction temperature (reaction conditions: WHSV = 6.8 h⁻¹, H₂/ n -C₇ molar ratio = 10, and atmospheric hydrogen pressure). (b) C₇ isomer yield (mol%) vs. total n -C₇ conversion (including cracking), plotted while increasing reaction temperatures. Arrows indicate “maximum obtainable i -C₇ mole percent”.

Table 3
Product distributions (mol%) at approximately 70% n -C₇ conversion over Pt(IE)/MFI zeolites.

Conv. (%) ^a	B-300	C-40	NC-10	NS-2
C ₁	0.5	0.9	1.1	0.5
C ₂	1.1	1.5	1.8	0.7
C ₃	35.4	34.9	17.7	18.0
i -C ₄	32.8	32.3	15.5	16.8
n -C ₄	2.2	2.2	2.2	1.0
C ₅	1.2	1.5	1.8	0.7
C ₆	0.5	0.8	1.1	0.5
2-MC ₆	16.9	13.7	27.9	26.6
3-MC ₆	8.8	9.5	22.3	26.8
2,3-DMC ₅	0.0	0.8	2.7	2.3
2,4-DMC ₅	0.4	1.2	3.7	4.5
2,2-DMC ₅	0.0	0.2	0.8	0.6
3,3-DMC ₅	0.0	0.1	0.3	0.1
EC ₅	0.1	0.3	1.0	1.0

^a MC₆, DMC₅, and EC₅ indicate methylhexane, dimethylpentane, and ethylpentane, respectively.

is probably because the molecule is too bulky to form inside the MFI zeolite channels. Propane and butanes (mainly i -C₄) were obtained in equivalent molar ratios as the main cracking products for all catalysts. The equal molar ratios could be explained by the reaction mechanism in which the main cracking route is β -scission of the isomer products, not direct cracking of n -C₇ [11,29,48–52]. Probably, other n -alkane products could be formed by hydrogenolysis over Pt or via dimerization cracking pathways [53].

The results for the IE catalysts in Table 3 and Fig. 4 indicated that thin zeolite crystals were more promising than bulk zeolite for enhanced production of C₇ isomers. The C₇ isomer selectivity increased in the order of NS-2 > NC-10 > C-40 > B-300. This order was not consistent with acidity of the zeolite samples. As described in Section 3.1.1, the NS-2 zeolite exhibited the lowest concentration of the strongest Brønsted acids (corresponding to the 86 ppm peak in the ³¹P NMR spectrum) among all samples. NC-10 and C-40 possessed very similar concentrations of the two types

of strong acid sites. B-300 contained fewer strong acid sites than these two samples, but certainly much more of the strongest acids than NS-2. In other words, the strong acid site concentration increased in the order of NS-2 < B-300 < C-40 ≈ NC-10. Therefore, we can attribute the enhanced isomer selectivity of the thin zeolite crystals to facile diffusion of branched isomers before cracking can occur, as suggested in previous reports [6–15]. The internal structure of MFI zeolite consists of intersecting straight and sinusoidal channels with pore openings of ~0.55 nm. This pore system is believed to permit the entry of linear n -C₇ molecules (~0.43 nm in kinetic diameter) easily, but after isomerization, the exit becomes hindered to the increased kinetic diameters (at least 0.55 nm) (see Fig. S5, Supporting information) [54]. During their long residence time in the zeolite channels, the branched isomers could undergo further reaction into more highly branched isomers or could undergo cracking. It would be even more difficult for these highly branched isomers to migrate out, and they would be thus more susceptible to cracking [3,48,50–52]. Such consecutive reactions would decrease the i -C₇ yield. In the case of extremely thin nanosheet (e.g., NS-2), it is reasonable that the primary isomers could diffuse out from the interior of the zeolite crystal quickly before occurring subsequent kinetic processes that consumed branched i -C₇ products.

3.2.2. Effect of Pt-acid distance in Pt(Cl)/MFI catalyst series

As shown in Table 2, the catalyst samples prepared by Cl adsorbed hydrogen much less efficiently than did catalysts prepared by IE. In the case of nanosheet NS-2, Pt NPs with two different diameters ($d_{\text{TEM}} = 1.8$ nm in Cl, and 2.8 nm in IE*) were supported. These samples exhibited chemisorptions of 0.70 and 0.50 H/Pt, respectively. In the other samples, the hydrogen chemisorption decreased even further: 0.52 H/Pt in NC-10, 0.40 in C-40, and 0.36 in B-300. As judged by these data, the Pt/MFI catalysts prepared by Cl had much lower Pt metal dispersion than did the IE-prepared samples (H/Pt = 1.07–1.41). In addition to metal dispersion, the Cl and IE samples had Pt NP locations that were remarkably different. Specifically, Pt NPs were uniformly distributed within the crystal in the case of IE, whereas they were located on external surfaces in Cl. In Fig. 5a, the catalytic conversion of n -C₇ by the Pt(Cl)/MFI

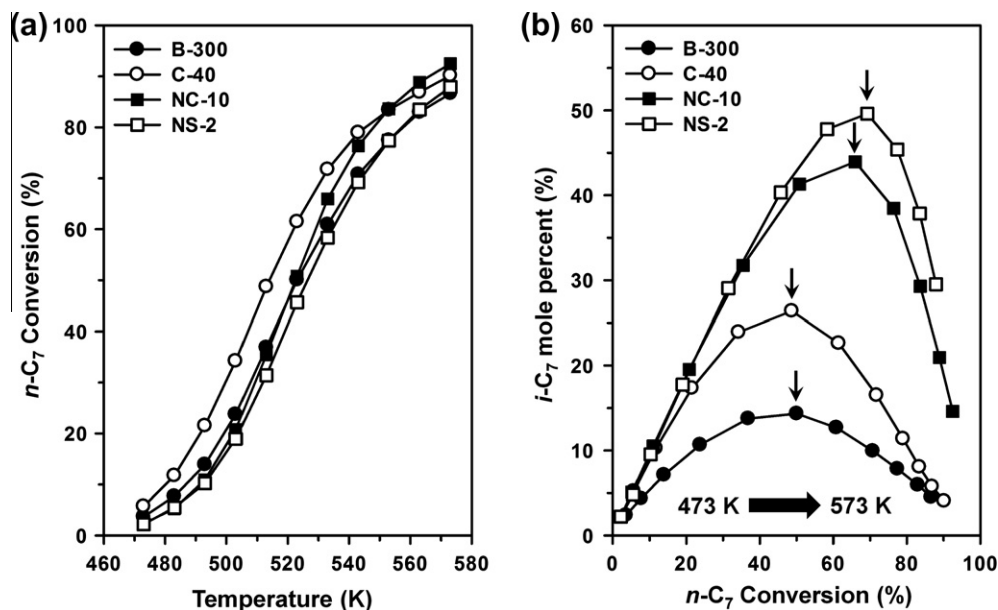


Fig. 5. (a) $n\text{-C}_7$ conversion by Pt(Cl)/MFI catalysts plotted as a function of reaction temperature (reaction conditions: WHSV = 6.8 h^{-1} , $\text{H}_2/n\text{-C}_7$ molar ratio = 10, and atmospheric hydrogen pressure). (b) C_7 isomer yield (mol%) vs. total $n\text{-C}_7$ conversion (including cracking), plotted while increasing reaction temperatures. Arrows indicate "maximum obtainable $i\text{-C}_7$ mole percent".

samples was plotted as a function of reaction temperature. These data were very similar to those for Pt(IE)/MFI (Fig. 4a). Thus, all of the Pt/MFI catalyst samples exhibited very similar $n\text{-C}_7$ conversion-vs.-temperature curves, despite significant differences in Pt NP location and particle size. Moreover, there were no significant differences between CI and CI* in NS-2, despite particle size differences (Pt NPs with $d_{\text{TEM}} = 1.0\text{ nm}$ by IE, 1.8 nm by CI, and 2.8 nm by CI*). This result indicated that all of the IE and CI catalyst samples had sufficient numbers of hydrogenating Pt sites that could balance the acidic function under the present reaction conditions. If the number of Pt sites had been insufficient, then the overall catalytic conversion would have been governed by Pt loading and dispersion [48–51].

In Fig. 5b, a correlation was obtained between total $n\text{-C}_7$ conversion and $i\text{-C}_7$ mole percent plotted as in Fig. 4b. Each plot showed a convex curve with a single maximum in the region of 45–75% conversion. The curve appearance was very similar to the result for Pt(IE)/MFI shown in Fig. 4b. A close examination of each pair of IE and CI samples prepared with the same zeolite (comparison of Figs. 4b and 5b) indicated that the two series of samples exhibited very similar results within the limits of experimental error, except for the case of Pt/B-300. In the case of Pt/B-300, the IE catalyst exhibited 22 mol% of $i\text{-C}_7$ at the maximum point. However, the Pt NPs supported by CI yielded only 14 mol%. Fig. 6 re-plots the maximum $i\text{-C}_7$ mole percent for all samples prepared by IE and CI methods with various crystal thicknesses. As reiterated in this figure, there were no significant differences in the maximum $i\text{-C}_7$ mole percent between each pair of CI and IE catalysts prepared with the same zeolite, except for the B-300 zeolite. Even in the case of B-300, the difference between CI and IE was much smaller than the difference in maximum $i\text{-C}_7$ mole percent between Pt(IE)/B-300 and Pt(IE)/NS-2. Thus, the isomer selectivity change due to a difference in Pt NP location was not so significant as the effect coming from the variation of zeolite crystal thickness. Mechanistically, it has been accepted that alkene intermediates are formed on Pt NPs by dehydrogenation, followed by isomerization or β -scission on acid sites [2–4,16]. Hydrogenation on Pt NPs subsequently generates corresponding alkane products. According to this bifunctional catalytic mechanism, the hydrogenation–dehydrogenation

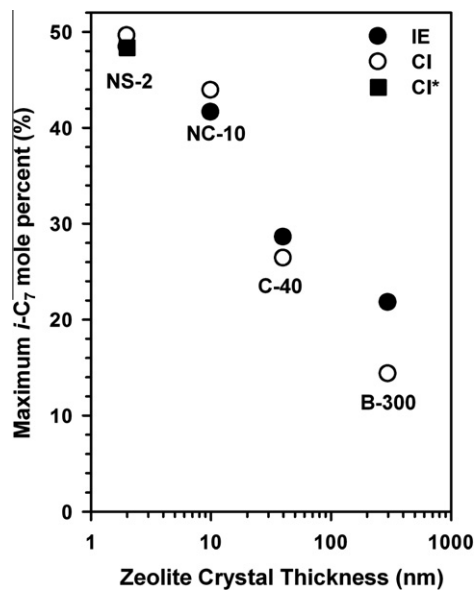


Fig. 6. Summary of maximum isomer yield.

function of the CI catalysts can be achieved exclusively on external surfaces where Pt NPs are located, while the resulting alkene intermediates migrate to the internal acid sites (and also those on external surfaces if they are sufficiently strong) for protonation and subsequent isomerization, which are the rate-determining steps. In this regard, if a CI catalyst is prepared with very thick zeolite crystals, the length of the diffusion path of alkenes is anticipated to influence both $n\text{-C}_7$ conversion and isomer yield. It seems that the zeolite crystal thickness that can cause such diffusion effects should be larger than 300 nm.

3.2.3. Comparison with $n\text{-C}_6$ hydroisomerization

Effects of zeolite crystal thickness and platinum location were also investigated in $n\text{-C}_6$ hydroisomerization. The reaction condi-

tions were the same as those for *n*-C₇ hydroisomerization, except for the use of low WHSV of *n*-C₆ (6.5 h⁻¹) and high reaction temperature (513–603 K). The B-300 and NS-2 samples were compared as supports for Pt NPs, in order to maximize the zeolite crystal thickness difference. Both the IE and CI methods were used to support Pt NPs on each zeolite. In this manner, we prepared four Pt/MFI catalyst samples with different crystal thicknesses and Pt NP locations. However, these catalyst samples exhibited very similar *n*-C₆ catalytic conversion and *i*-C₆ selectivity (see Fig. S6, Supporting information). From this result, we could confirm that these samples had both sufficient acids and sufficient Pt for the bifunctional catalysis required in hydroisomerization [55–58]. A notable difference from the case of *n*-C₇ was that the *i*-C₆ mole percent increased continuously with increasing reactant conversion, whereas the *n*-C₇ hydroisomerization followed a convex curve (Figs. 4b and 5b). This result indicated that hydrocracking reactions were not severe in the case of *n*-C₆, even under elevated temperature. For this reason, the isomer selectivity in *n*-C₆ hydroisomerization did not vary conspicuously as a function of zeolite crystal thickness and Pt-acid distance. The low hydrocracking tendency was consistent with a proposed reaction mechanism involving protonated cyclopropanes, which were energetically less favorable to undergo cracking for *n*-C₆ than in the case of *n*-C₇ [29]. It is therefore expected that the effect of the zeolite crystal thickness would be more remarkable in hydroisomerization of hydrocarbons higher than C₇.

4. Conclusions

In the present work, MFI zeolites of various crystal thicknesses were supported with Pt nanoparticles (NPs). In one series of samples, Pt NPs were uniformly supported within zeolite crystals by the ion-exchange (IE) technique. In another series, Pt NPs were supported on external surfaces of the crystal using the colloidal impregnation (CI) procedure. In both series, the experimental conditions for Pt loading and reaction measurement were chosen, so that all of the catalyst samples had sufficient numbers of hydrogenating Pt sites to balance acid catalysis in MFI zeolite for the hydroisomerization of *n*-heptane. Under these conditions, it was possible to investigate the effects of the zeolite crystal thickness and Pt locations on selectivity for branched heptanes (i.e., *i*-C₇).

The catalyst characterization data indicated that within the IE series of Pt/MFI, all samples maintained a similar close proximity between Pt NPs and acid sites. As the crystal thickness decreased from 300 to 2 nm, *i*-C₇ selectivity increased continuously by a factor of 2.2. The acidity of the zeolite samples was carefully investigated using NH₃ TPD and ³¹P NMR spectroscopy of adsorbed phosphine oxide. However, no correlations were observed between acidity and *i*-C₇ selectivity. Therefore, the low selectivity of bulk zeolite might be attributed to diffusion limitations of branched isomers and consecutive reactions to cracked products.

In the CI series of catalysts, the distance between Pt NPs and acid sites was systematically varied according to the zeolite crystal thickness, which was in contrast to the IE series. Nevertheless, except for the thickest zeolite sample (B-300), there were no conspicuous differences in *i*-C₇ selectivity between each pair of CI and IE catalysts prepared with the same zeolite. Even in the case of B-300, the selectivity difference between CI and IE was much smaller than the aforementioned nanosheet-bulk difference within the IE series. Thus, the isomer selectivity change due to a difference in Pt NP location between IE and CI was not so conspicuous as the effect coming from the variation of zeolite crystal thickness over the 2–300 nm range. This information would be useful for the rational design of hydroisomerization catalysts based on hierarchically porous zeolites. The most notable result was that product selectivity

could be continuously increased by decreasing the zeolite crystal thickness to 2 nm.

Acknowledgments

This work was supported by the Research Center Program (CA1201) of IBS (Institute for Basic Science) in Korea. The authors thank the National Nanofab Center for STEM measurement.

Appendix A. Supplementary material

Supplementary data associated with this article can be found, in the online version, at <http://dx.doi.org/10.1016/j.jcat.2013.02.015>.

References

- [1] G.W. Huber, S. Iborra, A. Corma, Chem. Rev. 106 (2006) 4044.
- [2] V.M. Akhmedov, S.H. Al-Khowaiter, Catal. Rev. 49 (2007) 33.
- [3] A. Deldari, Appl. Catal. A: Gen. 293 (2005) 1.
- [4] Y. Ono, Catal. Today 81 (2003) 3.
- [5] J. Pérez-Ramírez, C.H. Christensen, K. Egeblad, C.H. Christensen, J.C. Groen, Chem. Soc. Rev. 37 (2008) 2530.
- [6] M.S. Holm, E. Taarning, K. Egeblad, C.H. Christensen, Catal. Today 168 (2011) 3.
- [7] S. van Donk, A.H. Janssen, J.H. Bitter, K.P. de Jong, Catal. Rev. 45 (2003) 297.
- [8] A. Chica, A. Corma, J. Catal. 187 (1999) 167.
- [9] M. Tromp, J.A. van Bokhoven, M.T. Garriga Oostenbrink, J.H. Bitter, K.P. de Jong, D.C. Koningsberger, J. Catal. 190 (2000) 209.
- [10] S. van Donk, A. Broersma, O.L.J. Gijzeman, J.A. van Bokhoven, J.H. Bitter, K.P. de Jong, J. Catal. 204 (2001) 272.
- [11] A. Aerts, W. Huybrechts, S.P.B. Kremer, C.E.A. Kirschhock, E. Theunissen, A.V. Isacker, J.F.M. Denayer, G.V. Baron, J.W. Thybaut, G.B. Marin, P.A. Jacobs, J.A. Martens, Chem. Commun. (2003) 1888.
- [12] C.H. Christensen, I. Schmidt, C.H. Christensen, Catal. Commun. 5 (2004) 543.
- [13] Y. Fan, H. Xiao, G. Shi, H. Liu, X. Bao, J. Catal. 285 (2012) 251.
- [14] D.L. Moushey, P.G. Smirniotis, Catal. Lett. 129 (2009) 20.
- [15] A. Chica, U. Diaz, V. Fornés, A. Corma, Catal. Today 147 (2009) 179.
- [16] P.B. Weisz, Adv. Catal. 13 (1962) 137.
- [17] J. Čejka, H. van Bekkum, A. Corma, F. Schüth, Introduction to Zeolite Science and Practice, third ed., Elsevier Science, 2007.
- [18] J.A. Schwarz, C. Contescu, A. Contescu, Chem. Rev. 95 (1995) 477.
- [19] E. Iglesia, D.G. Barton, J.A. Biscardi, M.J.L. Gines, S.L. Soled, Catal. Today 38 (1997) 339.
- [20] K. Fujimoto, K. Maeda, K. Aimoto, Appl. Catal. A: Gen. 91 (1992) 81.
- [21] H.Y. Chu, M.P. Rosynek, J.H. Lunsford, J. Catal. 178 (1998) 352.
- [22] M. Höchtl, A. Jentys, H. Vinek, J. Catal. 190 (2000) 419.
- [23] M. Choi, K. Na, J. Kim, S. Yasuhiro, T. Osamu, R. Ryoo, Nature 461 (2009) 246.
- [24] K. Na, W. Park, Y. Seo, R. Ryoo, Chem. Mater. 23 (2011) 1273.
- [25] X. Zhang, D. Liu, D. Xu, S. Asahina, K.A. Cychosz, K.V. Agrawal, Y. Al Wahedi, A. Bhan, S. Al Hashimi, O. Terasaki, M. Thommes, M. Tsapatsis, Science 336 (2012) 1684.
- [26] R.M. Rioux, H. Song, J.D. Hoefelmeyer, P. Yang, G.A. Somorjai, J. Phys. Chem. B 109 (2005) 2192.
- [27] H. Song, R.M. Rioux, J.D. Hoefelmeyer, R. Komor, K. Niesz, M. Grass, P. Yang, G.A. Somorjai, J. Am. Chem. Soc. 128 (2006) 3027.
- [28] G.A. Somorjai, H. Frei, J.Y. Park, J. Am. Chem. Soc. 131 (2009) 16589.
- [29] S.T. Sie, Ind. Eng. Chem. Res. 32 (1993) 403.
- [30] K. Na, M. Choi, R. Ryoo, J. Mater. Chem. 19 (2009) 6713.
- [31] A.C.M. van den Broek, J. van Grondelle, R.A. van Santen, J. Catal. 167 (1997) 417.
- [32] A. Philippaerts, S. Paulussen, S. Turner, O.I. Lebedev, G.V. Tendeloo, H. Poelman, M. Bulut, F.D. Clippel, P. Smeets, B. Sels, P. Jacobs, J. Catal. 270 (2010) 172.
- [33] A. Philippaerts, S. Paulussen, A. Breesch, S. Turner, O.I. Lebedev, G.V. Tendeloo, B. Sels, P. Jacobs, Angew. Chem., Int. Ed. 50 (2011) 3947.
- [34] Y. Wang, J. Ren, K. Deng, L. Gui, Y. Tang, Chem. Mater. 12 (2000) 1622.
- [35] J. Kim, M. Choi, R. Ryoo, J. Catal. 269 (2010) 219.
- [36] E.F. Rakiewicz, A.W. Peters, R.F. Wormsbecher, K.J. Sutovich, K.T. Mueller, J. Phys. Chem. B 102 (1998) 2890.
- [37] Q. Zhao, W.-H. Chen, S.-J. Huang, Y.-C. Wu, H.-K. Lee, S.-B. Liu, J. Phys. Chem. B 106 (2002) 4462.
- [38] S. Zhang, S.-L. Chen, P. Dong, G. Yuan, K. Xu, Appl. Catal. A: Gen. 332 (2007) 46.
- [39] J.H. Sinfelt, D.J.C. Yates, J. Catal. 10 (1968) 362.
- [40] S.J. Cho, W.-S. Ahn, S.B. Hong, R. Ryoo, J. Phys. Chem. 100 (1996) 4996.
- [41] B.J. Kip, F.B.M. Duivenvoorden, D.C. Koningsberger, R. Prins, J. Catal. 105 (1987) 26.
- [42] F.W.H. Kampers, C.W.R. Engelen, J.H.C. van Hooff, D.C. Koningsberger, J. Phys. Chem. 94 (1990) 8574.
- [43] Z. Kónya, E. Molnar, G. Tasi, K. Niesz, G.A. Somorjai, I. Kiricsi, Catal. Lett. 113 (2007) 19.
- [44] J.N. Kuhn, C.-K. Tsung, W. Huang, G.A. Somorjai, J. Catal. 265 (2009) 209.
- [45] M. Rivallan, S. Thomas, M. Lepage, N. Takagi, H. Hirata, F. Thibault-Starzyk, ChemCatChem 2 (2010) 1599.

- [46] J.A. Lopez-Sanchez, N. Dimitratos, C. Hammond, G.L. Brett, L. Kesavan, S. White, P. Miedziak, R. Tiruvalam, R.L. Jenkins, A.F. Carley, D. Knight, C.J. Kiely, G.J. Hutchings, *Nature Chem.* 3 (2011) 551.
- [47] C. Aliaga, J.Y. Park, Y. Yamada, H.S. Lee, C.-K. Tsung, P. Yang, G.A. Somorjai, *J. Phys. Chem. C* 113 (2009) 6150.
- [48] M. Guisnet, F. Alvarez, G. Giannetto, G. Perot, *Catal. Today* 1 (1987) 415.
- [49] A. Patrigeon, E. Benazzi, Ch. Travers, J.Y. Bernhard, *Catal. Today* 65 (2001) 149.
- [50] A. Lugstein, A. Jentys, H. Vinek, *Appl. Catal. A: Gen.* 166 (1998) 29.
- [51] S. Gopal, P.G. Smirniotis, *J. Catal.* 225 (2004) 278.
- [52] T.L.M. Maesen, M. Schenk, T.J.H. Vlugt, B. Smit, *J. Catal.* 203 (2001) 281.
- [53] E. Blomsma, J.A. Martens, P.A. Jacobs, *J. Catal.* 155 (1995) 141.
- [54] E.B. Webb III, G.S. Grest, M. Mondello, *J. Phys. Chem. B* 103 (1999) 4949.
- [55] A. van de Runstraat, J.A. Kamp, P.J. Stobbelaar, J. van Grondelle, S. Krijnen, R.A. van Santen, *J. Catal.* 171 (1997) 77.
- [56] F.J.M.M. de Gauw, J. van Grondelle, R.A. van Santen, *J. Catal.* 206 (2002) 295.
- [57] J. Macht, R.T. Carr, E. Iglesia, *J. Am. Chem. Soc.* 131 (2009) 6554.
- [58] H. Chiang, A. Bhan, *J. Catal.* 283 (2011) 98.